SN 2020jgb: A Peculiar Type Ia Supernova Triggered by a Massive Helium-Shell Detonation in a Star-Forming Galaxy

Chang Liu [ID],[1] Adam A. Miller [ID],[1] Anya E. Nugent [ID],[1] Abigail Polin [ID],[2,3] Kishalay De [ID],[4,*]
Shreya Anand [ID],[5] Igor Andreoni [ID],[6,7,8,†] Thomas G. Brink [ID],[9] Suhail Dhawan [ID],[10] Alexei V. Filippenko [ID],[9]
Kate Maguire [ID],[11] Tassilo Schweyer [ID],[12] Yashvi Sharma [ID],[13] Steven L. Groom [ID],[14] David Hale,[15]
Frank J. Masci [ID],[14] Josiah Purdum [ID],[15] Benjamin Racine [ID],[16] Jesper Sollerman [ID],[12] and
Shrinivas R. Kulkarni [ID][13]

[1] *Center for Interdisciplinary Exploration and Research in Astrophysics (CIERA), Department of Physics and Astronomy, Northwestern University, 1800 Sherman Road, Evanston, IL 60201, USA*
[2] *The Observatories of the Carnegie Institution for Science, 813 Santa Barbara Street, Pasadena, CA 91101, USA*
[3] *TAPIR, Walter Burke Institute for Theoretical Physics, 350-17, Caltech, Pasadena, CA 91125, USA*
[4] *MIT-Kavli Institute for Astrophysics and Space Research, 77 Massachusetts Ave., Cambridge, MA 02139, USA*
[5] *Cahill Center for Astrophysics, California Institute of Technology, Pasadena CA 91125, USA*
[6] *Joint Space-Science Institute, University of Maryland, College Park, MD 20742, USA.*
[7] *Department of Astronomy, University of Maryland, College Park, MD 20742, USA.*
[8] *Astrophysics Science Division, NASA Goddard Space Flight Center, Mail Code 661, Greenbelt, MD 20771, USA*
[9] *Department of Astronomy, University of California, Berkeley, CA 94720-3411, USA*
[10] *Institute of Astronomy and Kavli Institute for Cosmology, University of Cambridge, Madingley Road, Cambridge CB3 0HA, UK*
[11] *School of Physics, Trinity College Dublin, The University of Dublin, Dublin 2, Ireland*
[12] *The Oskar Klein Centre, Department of Astronomy, Stockholm University, AlbaNova, SE-106 91 Stockholm, Sweden*
[13] *Division of Physics, Mathematics, and Astronomy, California Institute of Technology, Pasadena, CA 91125, USA*
[14] *IPAC, California Institute of Technology, 1200 E. California Blvd, Pasadena, CA 91125, USA*
[15] *Caltech Optical Observatories, California Institute of Technology, Pasadena, CA 91125, USA*
[16] *Aix Marseille Univ, CNRS/IN2P3, CPPM, Marseille, France*

ABSTRACT

The detonation of a thin ($\lesssim 0.03\,\mathrm{M_\odot}$) helium shell (He-shell) atop a white dwarf (WD) is a promising mechanism to explain normal Type Ia supernovae (SNe Ia), while thicker He-shells ($>0.03\,\mathrm{M_\odot}$) may explain some recently observed peculiar SNe Ia. We present observations of SN 2020jgb, a peculiar SN Ia discovered by the Zwicky Transient Facility (ZTF). Near maximum light, SN 2020jgb is subluminous (ZTF g-band absolute magnitude $M_g \approx -18.2\,\mathrm{mag}$) and shows an unusually red color ($g_{\mathrm{ZTF}} - r_{\mathrm{ZTF}} \approx 0.4\,\mathrm{mag}$) due to the strong line-blanketing blueward of $\sim 5000\,\text{Å}$. These properties resemble those of SN 2018byg, a peculiar SN Ia resulting from a "thick He-shell" double detonation (DDet). Using detailed radiative transfer models, we show that the optical spectroscopic and photometric evolution of SN 2020jgb are broadly consistent with a He-shell of $\sim 0.08\,\mathrm{M_\odot}$ detonating above a carbon-oxygen WD of $\sim 0.87\,\mathrm{M_\odot}$. We detect a prominent absorption feature at $\sim 1\,\mu\mathrm{m}$ in the near-infrared (NIR) spectrum of SN 2020jgb, which could originate from the unburnt helium in the outermost ejecta. While the sample size is limited, similar $1\,\mu\mathrm{m}$ features have been detected in all the thick He-shell DDet candidates with NIR spectra obtained to date. SN 2020jgb is also the first thick He-shell DDet SN discovered in a star-forming galaxy, indisputably showing that He-shell DDet objects occur in both star-forming and passive galaxies, consistent with the normal SN Ia population.

Keywords: Supernovae (1668), Type Ia supernovae (1728), White dwarf stars (1799), Observational astronomy (1145), Surveys (1671)

1. INTRODUCTION

It has been clear for decades that Type Ia supernovae (SNe Ia) are caused by the thermonuclear explosions of

* NASA Einstein Fellow
† Neil Gehrels Fellow

carbon-oxygen (C/O) white dwarfs (WDs) in binary systems (see Maoz et al. 2014, for a review). Nevertheless, the nature of the binary companion, as well as how it ignites the WD, remains highly uncertain.

The helium-shell (He-shell) double detonation (DDet) scenario is one of the most promising channels to produce SNe Ia. In this scenario, the WD accretes from a companion to develop a helium-rich shell, which, after becoming sufficiently massive, could detonate. Such a detonation sends a shock wave into the C/O core to trigger a runaway thermonuclear explosion that inevitably disrupts and destroys the entire WD (Nomoto 1982a,b; Woosley et al. 1986; Livne 1990; Woosley & Weaver 1994; Livne & Arnett 1995). This DDet mechanism can produce explosions of WDs below the Chandrasekhar-mass ($M_{\rm Ch}$).

There are several observational benchmarks for He-shell DDet SNe. Shortly after the ignition of the He-shell, the decay of radioactive material in the helium ashes may power a detectable flash (Woosley & Weaver 1994; Fink et al. 2010; Kromer et al. 2010). The Fe-group elements in the ashes will blanket blue photons with wavelengths $\lesssim 5000$ Å (Kromer et al. 2010), the duration of which depends on the mass of the He-shell. For shells that are sufficiently thick, Boyle et al. (2017) suggest that the unburnt helium could provide an observational signal in near-infrared (NIR) spectra, and Polin et al. (2021) predict significant [Ca II] emission in the nebular phase of the SNe.

Using different sets of He-shell mass and C/O core mass, one can reproduce a variety of observables in "normal" SNe Ia with typical luminosities and spectral features near peak light (e.g., Polin et al. 2019; Shen et al. 2021), or peculiar subluminous ones (e.g., Polin et al. 2019).

For the DDet SNe that show "normal" characteristics near peak brightness, the mass of the He-shell is expected to be low ($\lesssim 0.03\,{\rm M_\odot}$; Kromer et al. 2010; Sim et al. 2010; Shen et al. 2018; Polin et al. 2019). The first reported He-shell DDet candidate with a thin He-shell was SN 2016jhr (Jiang et al. 2017), which exhibits an early red flash and keeps a red $g-r$ color throughout its evolution, though it shows a typical absolute magnitude at peak ($M_g \approx -19$ mag) for normal SNe Ia. The multi-band light curves involving the early flash and the major peak, as well as the optical spectrum close to peak light, could be simultaneously fit by a near-$M_{\rm Ch}$ DDet model (a $1.38\,{\rm M_\odot}$ C/O core and a $0.03\,{\rm M_\odot}$ He-shell). Recently, it was reported that SN 2018aoz (Ni et al. 2022a), an SN Ia showing a rapid redward color evolution within ~ 12 hr after first light, could be explained by a sub-$M_{\rm Ch}$ DDet model (a $1.05\,{\rm M_\odot}$ C/O core and a $0.03\,{\rm M_\odot}$

He-shell). After this red excess, the photometric evolution is consistent with that of normal SNe Ia, when the ashes of the thin He-shell become optically thin. However, some of its peak-time and nebular-phase spectral properties are not consistent with a He-shell DDet scenario (Ni et al. 2022b), making its nature debatable. To date, only a small fraction of SNe Ia have been discovered sufficiently early for possible detection of early flashes (e.g., Deckers et al. 2022). While there could be a large underlying population of normal SNe Ia triggered by He-shell DDet, currently it is hard to verify this scenario.

In contrast, if the He-shell mass is much greater than $0.03\,{\rm M_\odot}$, the ashes of the He-shell detonation could remain optically thick over a much more extended time, resulting in the red color and low luminosity near peak light. SN 2018byg (De et al. 2019) is a prototype of thick He-shell DDet SNe. During the late stages of preparing this paper, Dong et al. (2022a) presented another thick He-shell DDet candidate, SN 2016dsg, accompanied with an archival transient OGLE-2013-SN-079 (Inserra et al. 2015). All three candidates are faint, red, and show strong line-blanketing in maximum-light spectra. A tentative detection of unburnt helium in SN 2016dsg was also reported by Dong et al. (2022a). The small sample size to date suggests that thick He-shell events might be intrinsically rare.

It has been proposed that some, if not all, of the calcium-strong (Ca-rich) gap transients, a population of faint SNe with conspicuous [Ca II] emission in the nebular phase (Filippenko et al. 2003), also arise from He-shell DDet (Dessart & Hillier 2015; De et al. 2020; Polin et al. 2021). A subclass of Ca-rich transients resemble SNe Ia near peak light (termed Ca-Ia objects), marked by strong Si II absorption and the absence of optical He I lines. There are only three Ca-Ia objects (PTF 09dav, SN 2016hnk, and SN 2019ofm; De et al. 2020), all showing mild to strong line-blanketing in spectra, and hence could be He-shell DDet objects (e.g., Jacobson-Galán et al. 2020). Nonetheless, they also exhibit properties similar to those of other types of subluminous SNe Ia, such as the strong O I absorption widely seen in 91bg-like objects (Filippenko et al. 1992) but not prominent in other He-shell DDet candidates. PTF 09dav shows the weakest line-blanketing among the three and exhibits features that are attributed to some rare elements such as Sc II (Sullivan et al. 2011), which cannot be immediately explained by either He-shell DDet or deflagration models. SN 2016hnk could also be explained by the deflagration of a near-$M_{\rm Ch}$ WD (Galbany et al. 2019). In summary, the nature of Ca-Ia objects remains ambiguous.

In this paper, we present observations of another promising thick He-shell DDet candidate, SN 2020jgb. This peculiar SN Ia highly resembles SN 2018byg in photometric and spectroscopic properties, and exhibits a remarkable feature in the NIR spectrum that could be attributed to the unburnt helium. In Section 2, we report the observations of SN 2020jgb, which are analyzed in Section 3, where we show its similarities with other He-shell DDet SNe and discuss the tentative He I absorption features. We use a grid of He-shell DDet models to fit the data of SN 2020jgb, and present the results in Section 4.1. Then we expand our discussion to other He-shell DDet SNe, discussing the possibly ubiquitous absorption features in their NIR spectra near $1\,\mu m$ (Section 4.2) and their diversity in host environments (Section 4.3). We draw our conclusions in Section 5.

2. OBSERVATIONS

2.1. *Discovery*

SN 2020jgb was first discovered by the Zwicky Transient Facility (ZTF; Bellm et al. 2019a; Graham et al. 2019) on 2020 May 03.463 (UT dates are used throughout this paper; MJD 58972.463) with the 48-inch Samuel Oschin Telescope (P48) at Palomar Observatory. The automated ZTF discovery pipeline (Masci et al. 2019) detected SN 2020jgb using the image-differencing technique of Zackay et al. (2016). The candidate passed internal thresholds (e.g., Mahabal et al. 2019; Duev et al. 2019), leading to the production and dissemination of a real-time alert (Patterson et al. 2019) and the internal designation ZTF20aayhacx. It was detected with $g_{ZTF} = 19.86 \pm 0.15\,mag$ at $\alpha_{J2000} = 17^{h}53^{m}12^{s}.651$, $\delta_{J2000} = -00°51'21''.81$ and announced to the public by Fremling (2020). The host galaxy, PSO J175312.663+005122.078, is a dwarf galaxy, to which SN 2020jgb has a projected offset of only $0''.3$. The last nondetection limits the brightness to $r_{ZTF} > 20.7\,mag$ on 2020 April 27.477 (MJD 58966.477; 5.99 days before the first detection). This transient was classified as an SN Ia by Dahiwale & Fremling (2020).

2.2. *Host Galaxy Observations*

On 2022 March 31, two years after the transient faded, we took a spectrum of its host galaxy using the DEep Imaging Multi-Object Spectrograph (DEIMOS) on the Keck-II 10 m telescope (Faber et al. 2003), with a total integration time of 3200 s. It was reduced with the PypeIt Python package (Prochaska et al. 2020) and is displayed in Figure 7. The host exhibits strong, narrow emission lines including Hα, Hβ, [N II] $\lambda\lambda$6548, 6583, [O III] $\lambda\lambda$4959, 5007, and [S II] $\lambda\lambda$6716, 6731. By fitting all these emission features with Gaussian profiles, we ob-

tain an average redshift of $z = 0.0309 \pm 0.0003$. With the diagnostic emission line equivalent width (EW) ratios (log [N II]/H$\alpha = -1.19 \pm 0.07$ and log [O III]/H$\beta = 0.53 \pm 0.06$)[1], the host is consistent with star-forming galaxies in the Baldwin et al. (1981, hereafter BPT) diagram (see also Veilleux & Osterbrock 1987).

To estimate the distance modulus of SN 2020jgb, we first use the 2M++ model (Carrick et al. 2015) to obtain the peculiar velocity toward its host galaxy, PSO J175312.663+005122.078, to be $179 \pm 250\,km\,s^{-1}$. This, combined with the recession velocity in the frame of the cosmic microwave background[2] (CMB) $v_{CMB} = 9136\,km\,s^{-1}$, yields a net Hubble recession velocity of $9307 \pm 250\,km\,s^{-1}$. Adopting $H_0 = 70\,km\,s^{-1}\,Mpc^{-1}$, $\Omega_M = 0.3$, and $\Omega_\Lambda = 0.7$, we estimate the luminosity distance of SN 2020jgb to be 136.1 Mpc, equivalent to a distance modulus of $\mu = 35.66 \pm 0.06\,mag$.

2.3. *Optical Photometry*

SN 2020jgb was monitored in the g_{ZTF} and r_{ZTF} bands by ZTF as part of its ongoing Northern Sky Survey (Bellm et al. 2019b). We adopt a Galactic extinction of $E(B - V) = 0.404\,mag$ (Schlafly & Finkbeiner 2011), and correct all photometry using the Fitzpatrick (1999) extinction model. We assume there is no additional extinction in the host galaxy. This assumption is supported by the lack of Na I D absorption at the redshift of the host galaxy, though see Poznanski et al. (2011) for caveats on the use of Na I D absorption as a proxy for extinction.

The forced-photometry absolute light curves[3] in g_{ZTF} and r_{ZTF} are shown in Figure 1, where we display all measurements having a siginal-to-noise ratio (SNR) greater than 2. The light curves are reduced using the pipeline from Miller et al. (2022, in preparation); see also Yao et al. (2019).

2.4. *Optical Spectroscopy*

We obtained optical spectra of the object from ~ -10 days to $\sim +150$ days relative to the r_{ZTF}-band peak, using the Spectral Energy Distribution Machine (SEDM; Blagorodnova et al. 2018) on the automated 60 inch telescope (P60; Cenko et al. 2006) at Palomar Observatory, the Kast Double Spectrograph (Miller & Stone 1994) on the Shane 3 m telescope at Lick Observatory, the Andalucia Faint Object Spectrograph

---

[1] Here [N II] denotes the EW of the [N II] λ6583 line, and [O III] denotes the EW of the [O III] λ5007 line.

[2] https://ned.ipac.caltech.edu/velocity_calculator

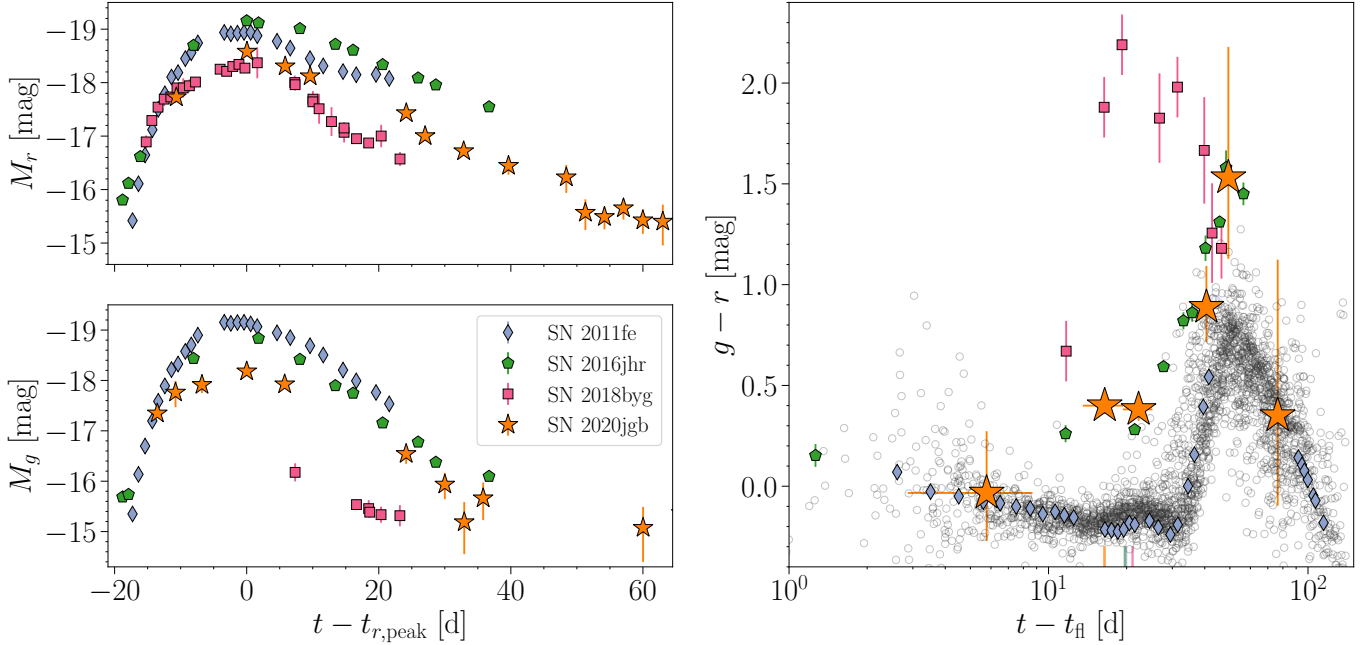[3] https://web.ipac.caltech.edu/staff/fmasci/ztf/forcedphot.pdf

Figure 1. Comparison of the photometric properties of SN 2020jgb with those of SN 2011fe (normal SN Ia; Pereira et al. 2013), SN 2016jhr (normal-luminosity He-shell DDet; Jiang et al. 2017), and SN 2018byg (subluminous He-shell DDet; De et al. 2019). *Left*: Multiband light curves. The upper (lower) panel shows the evolution in the r-band (g-band) absolute magnitude. *Right*: $g - r$ color evolution. For each object, the peak luminosity epoch is marked by a vertical line with the corresponding color on the bottom axis. The gray circles denote the $g_{\mathrm{ZTF}} - r_{\mathrm{ZTF}}$ color evolution of 62 normal SNe Ia (open circles) with prompt observations within 5 days of first light by ZTF (Bulla et al. 2020).

and Camera (ALFOSC)[4] installed at the Nordic Optical Telescope (NOT), the Double Beam Spectrograph (DBSP) on the 200 inch Hale telescope (P200; Oke & Gunn 1982), and the Low Resolution Imaging Spectrometer (LRIS) on the Keck-I 10 m telescope (Oke et al. 1995). With the exception of observations obtained with SEDM, all spectra were reduced using standard procedures (e.g., Matheson et al. 2000). The SEDM spectra were reduced using the custom `pysedm` software package (Rigault et al. 2019). Details of the spectroscopic observations are listed in Table 1, and the resulting spectral sequence is shown in Figure 2.

2.5. *Near-Infrared Spectroscopy*

We obtained one NIR (0.8–$2.5\,\mu$m) spectrum of SN 2020jgb using the Gemini near-infrared spectrometer (GNIRS; Elias et al. 1998) on the Gemini North telescope on 2020 June 9 ($\sim$22 days after r_{ZTF}-band peak), with an integration time of 2400 s. The GNIRS spectrum was reduced with `PypeIt`.

3. ANALYSIS

Table 1. Spectroscopic observations of SN 2020jgb and the host galaxy.

t_{obs}	Phase	Telescope/	R	Range	Airmass
(MJD)	(d)	Instrument	($\lambda/\Delta\lambda$)	(Å)	
58,976.42	−9.7	P60/SEDM	100	3770–9220	1.23
58,982.12	−4.2	NOT/ALFOSC	360	4000–9620	1.17
58,990.43	+3.9	P60/SEDM	100	3770–9220	1.23
58,997.44	+10.7	P60/SEDM	100	3770–9220	1.29
58,998.41	+11.6	Shane/Kast	750	3620–10720	1.28
59,008.41	+21.3	P60/SEDM	100	3770–9220	1.28
59,009.45	+22.4	Gemini-N/GNIRS	1800	8230–25150	1.07
59,010.40	+23.3	P200/DBSP	700	3200–9500	1.27
59,023.58	+36.1	Keck I/LRIS	1100	3200–10250	2.04
59,107.29	+117.3	Keck I/LRIS	1100	3200–10250	1.31
59,143.26	+152.2	Keck I/LRIS	1100	3200–10250	2.16
59,669.60	host	Keck II/DEIMOS	2100	4500–8700	1.14

NOTE—Phase is measured relative to the r_{ZTF}-band peak in the host galaxy rest frame. The resolution R is reported for the central region of the spectrum.

3.1. *Photometric Properties*

SN 2020jgb exhibited a fainter light curve than normal SNe Ia. In Figure 1, we compare the photometric properties of SN 2020jgb with the nearby, well-observed SN 2011fe with in synthetic photometry in g_{ZTF} and
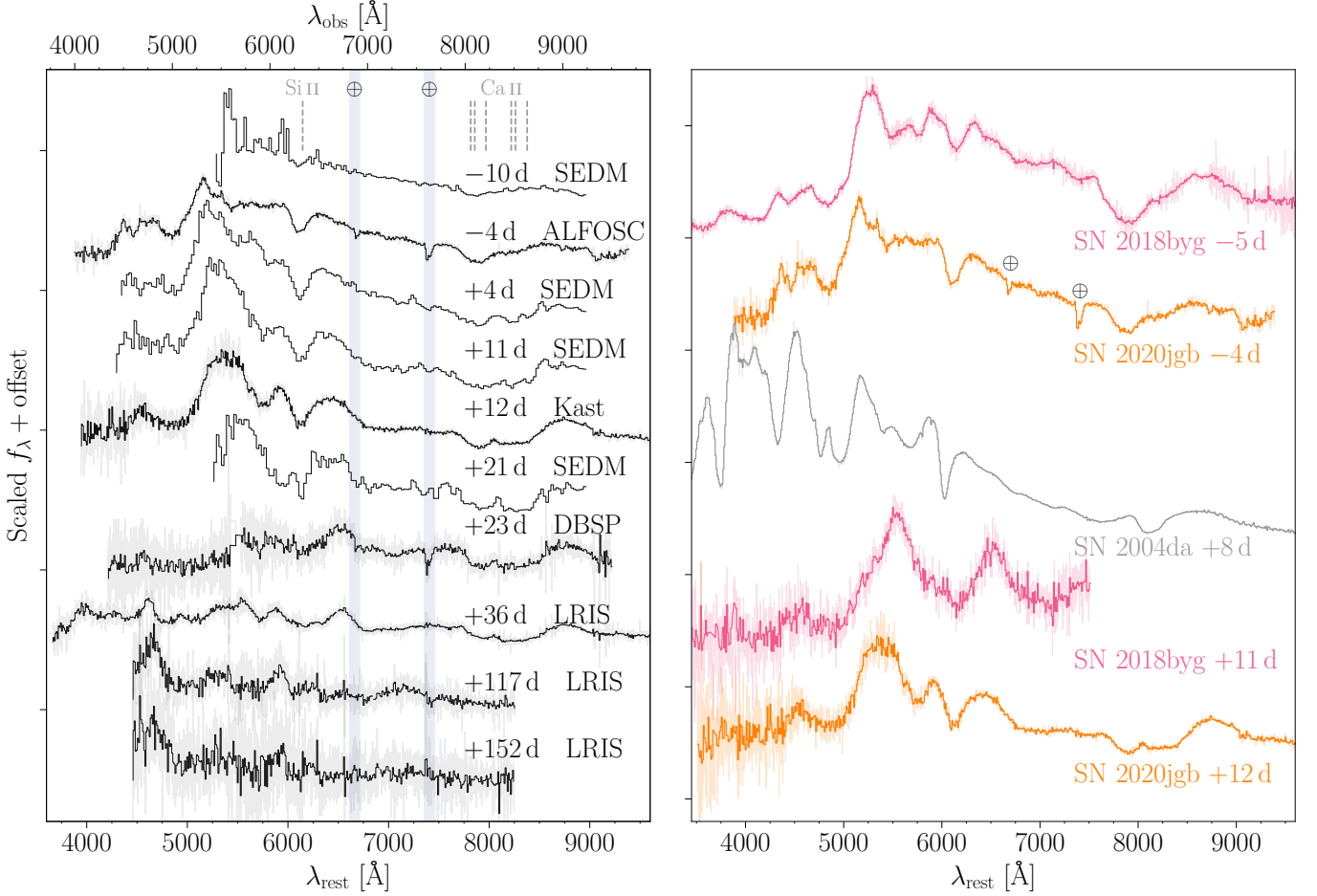
Figure 2. Optical spectra of SN 2020jgb, typical of a peculiar SN Ia triggered by He-shell DDet. *Left*: optical spectral sequence of SN 2020jgb. Rest-frame phases (days) relative to the $r_{\rm ZTF}$-band peak and instruments used are posted next to each spectrum. The spectra after Galactic extinction correction are shown in gray. The black lines are binned spectra with a bin size of 10 Å, except for the SEDM spectra, whose resolution is lower than the bin size. In the last two spectra, we have subtracted the light from the host galaxy. Only regions with SNR > 2.5 after binning are plotted. The corresponding wavelengths of the Si II λ6355 line (with an expansion velocity of $10{,}000\,{\rm km\,s^{-1}}$) and the Ca II IRT (with expansion velocities of both $10{,}000\,{\rm km\,s^{-1}}$ and $25{,}000\,{\rm km\,s^{-1}}$) are marked by the vertical dashed lines. *Right*: spectral comparison with SN 2018byg (subluminous He-shell DDet; De et al. 2019) and SN 2004da (normal luminosity; Silverman et al. 2012).

$r_{\rm ZTF}$ from the spectrophotometric time series of Pereira et al. (2013), as well as two He-shell DDet candidates, including the normal-luminosity thin He-shell candidate SN 2016jhr (Jiang et al. 2017) and the subluminous thick He-shell candidate SN 2018byg (De et al. 2019). All of these light curves have been corrected for Galactic reddening, while K-corrections have not been performed[5].

While the observational coverage is sparse in the rise to maximum light, from Figure 1 it is clear that SN 2020jgb is less luminous than normal SNe Ia (e.g., SN 2011fe). Furthermore, there is a flatter evolution in $r_{\rm ZTF}$ between $-14\,{\rm d}$ and maximum light for both SN 2020jgb and SN 2020jgb than there is for SN 2011fe.

In the right panel of Figure 1, we compare the color evolution $(g-r)$ of these objects relative to the measured time of first light $t_{\rm fl}$, accompanied by 62 normal SNe Ia (open circles) observed within 5 days of $t_{\rm fl}$ by ZTF (from Bulla et al. 2020). For SN 2020jgb, the early rise of the light curve was not well sampled, so we estimate $t_{\rm fl}$ as the midpoint of the first detection and the last nondetection. We adopt an uncertainty in this estimate of 3 days. All three He-shell DDet candidates are undoubtedly redder than normal SNe Ia. At peak light, SN 2020jgb ($g_{\rm ZTF} - r_{\rm ZTF} \approx 0.4\,{\rm mag}$) was not as red as the extreme case, SN 2018byg ($g-r \approx 2.2\,{\rm mag}$), but exhibited a similar color as SN 2016jhr ($g-r \approx 0.3\,{\rm mag}$).

---

[5] These SNe were all observed in slightly different g and r filters.

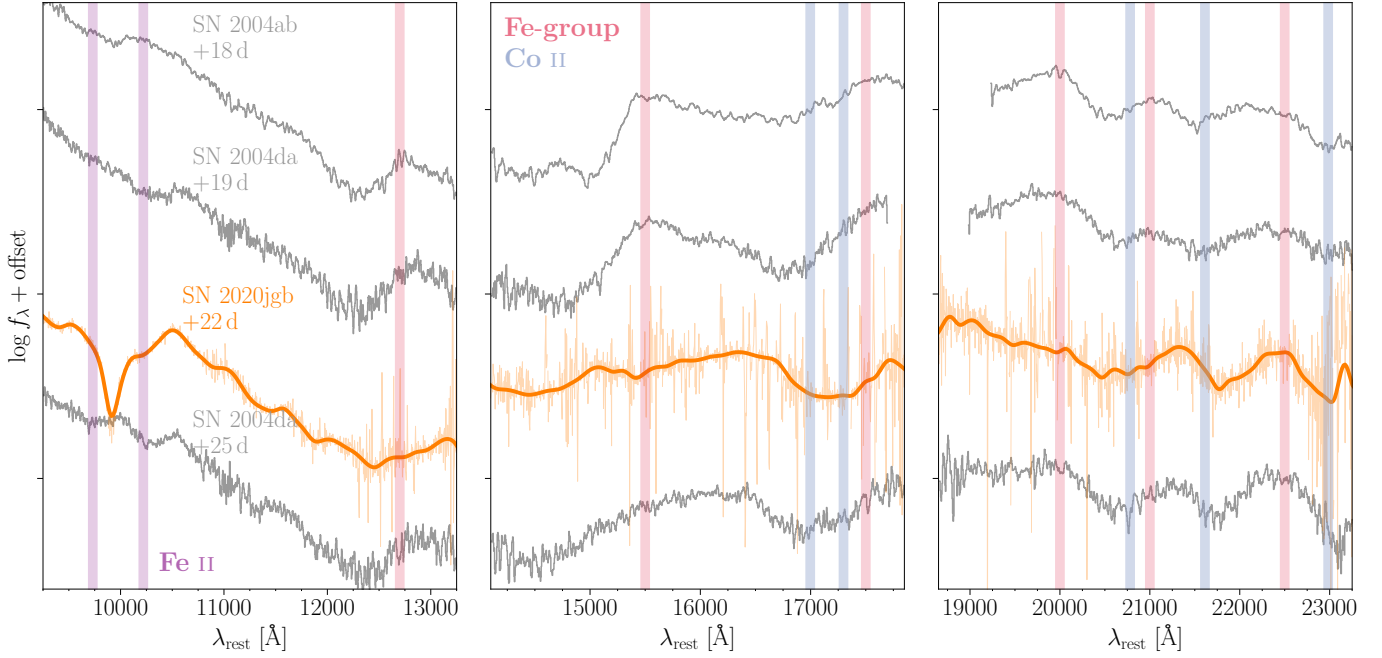### 3.2. *Optical Spectral Properties*

Figure 3. NIR spectra of SN 2020jgb and two normal-luminosity SNe Ia, SN 2004ab and SN 2004da (Marion et al. 2009), both showing highly similar spectral features except the absorption line near $1\,\mu$m. All spectra were obtained at similar phases. For each spectrum, the continuum at $\gtrsim 1.2\,\mu$m is significantly reshaped by the line-blanketing from Fe-group elements (red stripes), which are continuous emission features composed of unresolved Fe-group lines peaking at $\sim$1.27, 1.55, 1.75, 2.00, 2.10, and $2.25\,\mu$m (Marion et al. 2009). Between these peaks lie multiple strong Co II absorption lines (yellow stripes), for which a typical post-maximum expansion velocity of $8000\,\mathrm{km\,s^{-1}}$ is assumed. The purple stripes correspond to Fe II $\lambda 9998$ and Fe II $\lambda 10500$, also with an expansion velocity of $8000\,\mathrm{km\,s^{-1}}$.

In Figure 2, we show the optical spectral sequence of SN 2020jgb, and compare its spectra with those of some other SNe Ia at similar phases relative to peak brightness. For the spectra obtained after $+100\,$d there is clear contamination from the host galaxy, including the presence of narrow emission lines. For these spectra we subtract the galaxy light as measured in the DEIMOS spectrum from 2022 (see Section 2.4). The earliest spectrum was obtained by SEDM $\sim$10 days before r_{ZTF}-band peak. We only show portions of the spectrum where the SNR > 2.5, where the continuum is almost featureless with some marginal detection of the Si II $\lambda 6355$ at $\sim$6100 Å, the trademark of SNe Ia. In subsequent spectra the Si II features become more prominent and are clearly detected until $\sim$12 d after peak light. We measure Si II expansion velocities following a procedure similar to that of Childress et al. (2013, 2014) and Maguire et al. (2014). The fitting region is selected by visual inspection. The continuum is assumed to be linear, and the absorption profile after the continuum normalization is assumed to be composed of double Gaussian profiles centered at 6347 Å and 6371 Å. Within the model, the continuum flux density at the blue and red edges are free parameters for which we adopt a normal distribution as a prior. The mean and standard deviation for the

normal are the observed flux density and its uncertainty (respectively) at each edge of the fitting region. Three more parameters (amplitude, mean velocity, logarithmic velocity dispersion) are used to characterize the double-Gaussian profile, whose priors are set to be flat. This means the depths and widths of both peaks are forced to be the same, as Maguire et al. (2014) adopted in the optically thick regime. The posteriors of the five parameters are sampled simultaneously with emcee (Foreman-Mackey et al. 2013) using the Markov chain Monte Carlo (MCMC) method. We find that the mean expansion velocity is $\sim$11,500 $\mathrm{km\,s^{-1}}$ near maximum light.

In many SNe Ia, the Ca II near-infrared triplet (Ca II IRT) $\lambda\lambda 8498$, 8542, 8662. absorption has two distinct components (Mazzali et al. 2005), which are conventionally referred to as photospheric-velocity features (PVFs) and high-velocity features (HVFs). The PVFs originate from the main line-forming region with typical photospheric (i.e., bulk ejecta) velocities, while the HVFs are blueshifted to much shorter wavelengths, indicating significantly higher (by greater than $\sim$6000 $\mathrm{km\,s^{-1}}$) velocities than typical PVFs (Silverman et al. 2015). Figure 2 shows that SN 2020jgb has prominent HVFs of Ca II IRT. The HVFs are visible in our first spectrum of SN 2020jgb, and remain prominent through $+36\,$days.

Using a similar technique in modeling the Si II features, we fit the HVFs and PVFs simultaneously. Both are fit by multiple Gaussian profiles assuming each line in the triplet can be approximated by the same profile (i.e., same amplitude and velocity dispersion). A best-fit expansion velocity of HVFs is $\sim$26,000 km s^{-1}. A clear delineation between the HVFs and PVFs is visible $\sim$4 days before peak light. Since then we fit the broad absorption features with two different velocity components simultaneously. From $\sim$$-5$ d to $\sim$$+20$ d, the velocity of HVFs slightly declines but stays above $\sim$24,000 km s^{-1}, and the velocity of PVFs declines from $\sim$11,000 km s^{-1} to $\sim$9,000 km s^{-1}. As in normal SNe Ia, the relative strength between the HVFs and PVFs decreases with time.

The optical spectral evolution of SN 2020jgb resembles that of SN 2018byg, a subluminous thick He-shell DDet SN. At early times, both SNe were relatively blue and featureless, with broad and shallow Ca II IRT absorption. As they evolved closer to maximum light, they developed strong continuous absorption blueward of $\sim$5000 Å, while Si II λ6355 and the Ca II IRT became more prominent. S II was not detected in either object. In the DDet scenario, a large amount of Fe-group elements would be synthesized in the outer regions of the ejecta, which would cause significant line-blanketing near maximum light (Kromer et al. 2010; Polin et al. 2019) and high-velocity intermediate-mass elements like Ca II (Fink et al. 2010; Kromer et al. 2010; Shen & Moore 2014). The similarity to SN 2018byg makes SN 2020jgb another promising He-shell DDet SN candidate.

SN 2004da is a normal SN Ia that shows similarities to SN 2020jgb in the NIR (Section 3.3); however, the two SNe are very different in the optical (Figure 2). From this comparison it is clear that SN 2020jgb is not a normal SN Ia.

The nebular-phase spectra of SN 2020jgb are dominated by Fe-group elements, showing some enhancement in flux between $\sim$4500 and $\sim$6000 Å. We did not detect any emission feature related to the [Ca II] $\lambda\lambda$7291, 7324 doublet, which is a hallmark for Ca-rich transients and is prominent in the two Ca-Ia objects, SN 2016hnk and SN 2019ofm (De et al. 2020). It is argued in (Polin et al. 2021) that for subluminous He-shell DDet SNe, the [Ca II] $\lambda\lambda$7291, 7324 doublet is expected to be prominent. If the total mass of the progenitor is sufficiently low ($\lesssim$0.9 M$_\odot$), the [Ca II] lines will completely dominate other coolants, such as the Fe-group lines, clearly in contrast to what we see in SN 2020jgb. We note that the [Ca II] features are not detected in SN 2018byg and SN 2016dsg either, though for both objects, the last

spectra were obtained at $\sim$$+50$ d. Even for subluminous objects with low ejecta masses, at such a phase the ejecta might still be in the transitional era before entering the true nebular phase.

3.3. *NIR Spectral Properties*

The NIR spectrum of SN 2020jgb is compared with those of two normal SNe Ia at a similar phase in Figure 3 (data for SNe 2004ab and 2004da from Marion et al. 2009). SN 2020jgb shows a strong absorption feature at $\sim$0.99 μm, which is not seen in normal SNe Ia. This feature was still significant two weeks later, as detected with LRIS on Keck (see Figure 6), though it was only partially covered. Aside from this prominent feature, SN 2020jgb resembles normal SNe Ia in the NIR. The shape of the continuum redward of $\sim$1.2 μm is significantly altered by line-blanketing from Fe-group elements. Just like normal SNe Ia, SN 2020jgb shows an enhancement of flux at about 1.3, 1.55, 2.0, 2.1, and 2.25 μm, accompanied by several Co II absorption lines. It is especially similar to SN 2004da at $+25$ days after maximum light as the steep increase in flux at $\sim$1.55 μm, known as the *H*-band break (Hsiao et al. 2019), has become less prominent.

Marion et al. (2009) presented a sample of 15 NIR spectra of normal SNe Ia between $+14$ and $+75$ days after maximum light, and none of those spectra show prominent absorption features around 1 μm. We have investigated several potential identifications for this feature (see below), none of which provides a completely satisfying explanation.

The most tantalizing possibility is that the absorption is due to He I λ10830. If SN 2020jgb is a He-shell DDet SN, then unburnt He could lead to observed absorption in the spectrum, as shown in the sub-$M_{\rm Ch}$ He-shell DDet models of Boyle et al. (2017). Figure 6 shows that the 1 μm feature, if associated with He I λ10830, has a velocity of $\sim$26,000 km s^{-1}. This aligns well where the helium lies in He-shell DDet models when the ejecta have reached homologous expansion (Kromer et al. 2010; Polin et al. 2019), yet it is unclear whether the high-velocity unburnt helium could stay optically thick until weeks after maximum light. The Ca II IRT also exhibits similarly high velocities at the same phase ($\sim$24,000 km s^{-1}), meaning that high-velocity absorption is not impossible at this phase. The expansion velocity in the ejecta is roughly linearly proportional to the radius, so such a high velocity indicates that both the Ca II IRT and the tentative He I absorption line form far outside the normal photosphere, which has a velocity of only $\sim$10,000 km s^{-1}. The two-dimensional (2-D) models of Kromer et al. (2010) also suggest that

helium may expand faster than the synthesized calcium in the He-shell. In this sense, the He-shell DDet scenario is supported because any unburnt helium would be located in the outermost ejecta.

We cannot claim an unambiguous detection of He I, however, as our spectra lack definitive absorption from other He I features that we would expect to be prominent, such as He I $\lambda20581$. Considering a line velocity of $\sim26,000\,\mathrm{km\,s^{-1}}$ and a host-galaxy redshift of 0.0309, this line will be blueshifted to $\sim1.95\,\mu m$ in the observer frame, which overlaps with some strong telluric lines within 1.8–$2.0\,\mu m$. After telluric correction, the SNR reaches ~5, with which we still cannot see any significant absorption feature. An upper limit of the equivalent width is determined to be $<2\%$ that of the He I $\lambda10830$ line, while theoretically, the $\lambda20581$ line is supposed to be only a factor of 6–12 weaker, depending on the temperature (Marion et al. 2009). The observed $1\,\mu m$ feature in SN 2020jgb is as strong as the He I $\lambda10830$ line in many helium-rich Type Ib supernovae (SNe Ib; see Filippenko 1997, for a review of SN spectral classification). In SNe Ib, the He I $\lambda20581$ line is weaker than the He I $\lambda10830$ line, yet still prominent (Shahbandeh et al. 2022). In one of the models of Boyle et al. (2017), there is no obvious He I $\lambda20581$ absorption in the synthetic spectra (see their Figure 7), but the model is intended to be representative of normal-luminosity SNe Ia. If the $1\,\mu m$ feature is associated with He I, it is unusual that we do not detect a corresponding feature around $2\,\mu m$.

Other possible identifications for the $1\,\mu m$ feature include Mg II $\lambda10927$, C I $\lambda10693$, and Fe II $\lambda10500$ and $\lambda10863$. The Mg II $\lambda10927$ line is prevalent in the NIR spectra of SNe Ia, but usually disappears within a week after peak brightness (Marion et al. 2009). In SN 2020jgb the $1\,\mu m$ feature was still visible more than a month after peak brightness in the Keck/LRIS spectrum. A Mg II $\lambda10927$ identification would require an absorption velocity of $\sim28,000\,\mathrm{km\,s^{-1}}$, $\sim20\%$ faster than the HVFs of Ca II IRT at the same phase. Such a high-velocity Mg II line has never been seen in other SNe Ia, and requires a high magnesium abundance in the outermost ejecta. However, the amount of magnesium synthesized in the detonation of the He-shell is expected to be tiny (Fink et al. 2010; Kromer et al. 2010; Polin et al. 2019, 2021). On the other hand, if we attribute this $1\,\mu m$ feature to high-velocity Mg II, we would expect an even stronger Mg II $\lambda9227$ line to be blueshifted to the red edge of the Ca II IRT, which is not detected. Given the strength of the $1\,\mu m$ feature, the Mg II $\lambda9227$ line should not be completely obscured by the Ca II IRT features.

C I $\lambda10693$ is not observed as frequently as Mg II $\lambda10927$ in SNe Ia. Hsiao et al. (2019) presented a sample of five SNe Ia with C I detections, showing that the C I feature is strongest for fainter, fast-declining objects. However, in their sample, the C I line is a pre-maximum feature which fades away as the luminosity peaks, so the discrepancy in phase is large. The required expansion velocity $\sim22,000\,\mathrm{km\,s^{-1}}$ is substantially faster than the estimated carbon velocity for the sample of Hsiao et al. (2019) ($\sim10,000$–$12,000\,\mathrm{km\,s^{-1}}$), but still consistent with the HVFs of Ca II IRT in SN 2020jgb. Nonetheless, no significant carbon absorption is detected in the optical. It is also noteworthy that the amount of unburnt carbon is expected to be minimal in sub-M_{Ch}WDs ignited by detonation (Polin et al. 2019), in contrast to near-M_{Ch} WDs ignited by pure deflagration where the carbon burning could be incomplete. We therefore would not expect to detect any carbon features in a He-shell DDet SN.

The Fe II features in SNe Ia usually start to develop approximately three weeks after peak brightness, which is about the same phase as we obtained our GNIRS spectrum. Two Fe II lines, $\lambda9998$ and $\lambda10500$, are actually visible on the blue/red wings of the $1\,\mu m$ feature. The Fe II $\lambda10863$ line is not detected in the GNIRS spectrum. SN 2004da shows very similar Fe II features near $1\,\mu m$, in which Fe II $\lambda10500$ is the strongest line ate this phase, as displayed in Figure 3. They correspond to an expansion velocity of $\sim8000\,\mathrm{km\,s^{-1}}$, which is consistent with the PVFs of the Ca II IRT at the same epoch. They also match the same two lines for normal SNe Ia (Marion et al. 2009), making the identification more reliable. Obviously, these two Fe II features are wider and shallower than the strong feature between them. We fit the $1\,\mu m$ feature with three Gaussian profiles. Two of them are set to be the blueshifted Fe II $\lambda9998$ and $\lambda10500$, and the other is an uncorrelated Gaussian profile which mainly describes the deep absorption feature in the center of the line complex. We find that the shallower and wider Fe II lines only make up $\sim40\%$ of the total equivalent width, and the remaining $\sim60\%$ comes from the central feature, which cannot be accounted for by any Fe II feature at the same velocity. Given the similarity of the Fe-group line-blanketing between the GNIRS spectrum with the spectrum of SN 2004da at $+25\,\mathrm{days}$, the distribution of Fe-group elements inside each SN ejecta should be somewhat similar, so the central region of the $1\,\mu m$ feature is not likely to be associated with Fe II either.

4. DISCUSSION

4.1. *Models*

We model SN 2020jgb using the methods outlined by Polin et al. (2019); the process is twofold. After choosing an initial model that describes a WD of a given mass with a choice of He-shell mass, we use the `CASTRO` code (Almgren et al. 2010) to perform a 1-D hydrodynamic simulation with simultaneous nucleosynthesis from the time of He-shell ignition through the secondary detonation and until the ejecta have reached homologous expansion ($\sim$10 s). At this point we take the ejecta profile (velocity, density, temperature and composition) and use the Monte Carlo radiative transport code `SEDONA` (Kasen et al. 2006) to calculate synthetic light curves and spectra of our model under the assumption of local thermal equilibrium (LTE).

In Figure 4, we show the comparison of the photometric and spectroscopic features of SN 2020jgb with DDet models from Polin et al. (2019). The peak luminosity reflects the total progenitor mass (C/O core + He-shell), and we find models with a total mass of $0.95\,M_\odot$ generally reproduce the $r_{\rm ZTF}$-band peak brightness well. All the models shown in Figure 4 reflect a total mass of $0.95\,M_\odot$. The overall photometric evolution in $r_{\rm ZTF}$ is best fit by the model with a $0.87\,M_\odot$ C/O core and a $0.08\,M_\odot$ He-shell, while all three models underestimate the $g_{\rm ZTF}$-band brightness after the peak. This deviation may be attributed to a variety of factors on handling the explosion and radiative transfer. First, throughout the simulations we assume local thermodynamic equilibrium (LTE), which is not valid once the ejecta become optically thin. Typically the bulk ejecta of a sub-$M_{\rm Ch}$ SN Ia remain optically thick for $\sim$30 days after the explosion. But in modeling the $g_{\rm ZTF}$-band brightness, the LTE assumption is even more tricky, because the major opacity in $g_{\rm ZTF}$ comes from the Fe-group line-blanketing in the outermost ejecta, where the optical depth may evolve differently from that at the photosphere. Hence, the LTE condition may quickly become inapplicable. Furthermore, our 1-D He-shell model is not capable of capturing multidimensional effects in the explosion such as asymmetries. The viewing angle is known to have a significant influence on the observed light curves (Kromer et al. 2010; Sim et al. 2012; Gronow et al. 2020; Shen et al. 2021), especially in bluer bands where the line-blanketing depends sensitively on the distribution of He-shell ashes (Shen et al. 2021). In previous studies of other He-shell DDet objects, the g-band brightness is systematically underpredicted shortly after the peak, despite the fact that redder bands can be fit decently (e.g., Jiang et al. 2017; Jacobson-Galán et al. 2020).

The model which best fits the photometry ($0.87\,M_\odot$ + $0.08\,M_\odot$) also reproduces the major absorption features (e.g., Fe-group line-blanketing, Si II λ6355, PVFs of

Ca II IRT) and the corresponding expansion velocities near peak light (see the right panel of Figure 4). However, we are not able to fit the continuum as well as the strong Ca II HVFs with the synthetic spectrum. These discrepancies could also be due to asymmetry in the DDet, if SN 2020jgb was observed fairly close to the ignition point, where the abundances of Fe-group elements and high-velocity calcium synthesized in the He-shell could be much higher than a spherical 1-D model would predict. In addition, the predicted Si II λ5972 does not show up in the observed spectrum.

Given the strong qualitative match between the observations of SN 2020jgb and the DDet models of Polin et al. (2019), and the similarity between SN 2020jgb and SN 2018byg, we conclude that SN 2020jgb is indeed a He-shell DDet event.

4.2. *The 1 μm Feature*

While the nature of the $1\,\mu$m feature remains uncertain, other He-shell DDet candidates show similar complexity in this region. In the currently small sample, only three objects (SN 2016hnk, SN 2018byg, and SN 2020jgb) have at least one available NIR spectrum (all obtained at different phases), each exhibiting strong absorption features near $1\,\mu$m, as shown in Figure 5. SN 2016hnk has two deep absorption features at $\sim$1.02 μm and $\sim$1.17 μm; both are at a longer wavelength than the $1\,\mu$m feature in SN 2020jgb. It is suggested in Galbany et al. (2019) that both of them are caused by Fe II, though they are deeper than in other SNe Ia. The velocity of the $1.02\,\mu$m feature is $\sim$21,000 km s^{-1} assuming a He I λ10830 origin, which, just like for SN 2020jgb, is about the same as the HVFs of the Ca II IRT (see Figure 6). The PVFs of the Ca II IRT of both SNe have a similar expansion velocity of $\sim$10,000 km s^{-1}. Such a consistency in velocities is also seen in SN 2018byg (see Figure 6). The large width and low SNR for the $1\,\mu$m feature in SN 2018byg make it difficult to determine an exact line velocity. The feature may be a mixture of several different lines in SN 2018byg.

Dong et al. (2022a) recently presented another thick He-shell DDet candidate, SN 2016dsg, with an absorption line around 0.97–1.05 μm in a low-SNR NIR spectrum at +16.6 days[6]. Assuming a He I λ10830 origin, the minimum of the absorption profile (at $\sim$1.03 μm; see Figure 4 of Dong et al. 2022a) corresponds to an expansion velocity of $\sim$15,000 km s^{-1}. Interestingly, SN 2016dsg shows the least prominent HVFs of Ca II

---

[6] SN 2016dsg was discovered on the decline. The phase is relative to the discovery time.
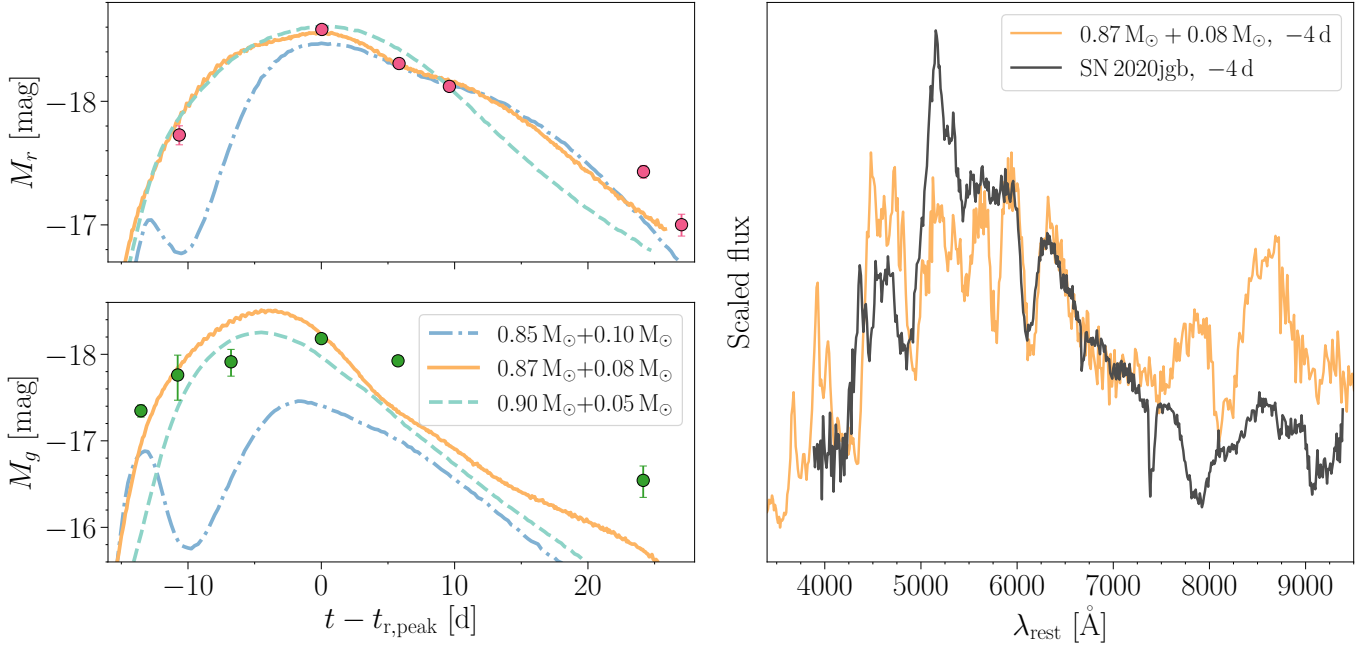
Figure 4. Spectrophotometric comparison of SN 2020jgb observations with a few He-shell DDet models from Polin et al. (2019). *Left:* Light-curve comparison. The model parameters are indicated in the legend as (C/O core mass + He-shell mass). The upper (lower) panel shows the evolution in the r_{ZTF}-band (g_{ZTF}-band) absolute magnitudes. *Right:* Comparison of the observed spectrum with the $0.87\,\mathrm{M_\odot}$ C/O core $+\,0.08\,\mathrm{M_\odot}$ He-shell model before peak luminosity. Each spectrum is normalized by the median flux between 6500 and 7500 Å, and binned with a size of 10 Å. The synthetic spectrum best matches the ALFOSC spectrum (Galactic extinction corrected), obtained ∼4 days before the r_{ZTF} peak. All of the phases have been rescaled to the host-galaxy rest frame.

IRT ($v_{\mathrm{SN\,2016dsg}} \approx 15{,}000\,\mathrm{km\,s^{-1}}$) among all the He-shell DDet candidates with NIR spectra. Once again, the scenario where both the unburnt helium and the high-velocity calcium are located at the outermost shell is favored.

Unfortunately, none of the spectra of SN 2016dsg, SN 2016hnk, or SN 2018byg cover the $2\,\mu$m region; thus, it is not possible to identify the presence of helium decisively. But if the $1\,\mu$m features of these objects are of the same origin, they are more likely to be correlated with the high-velocity ejecta lying in the outmost region in the SNe, because at least for SN 2020jgb, SN 2016dsg, and SN 2016hnk, the difference in their photospheric velocities cannot explain the discrepancy in their line velocities of the $1\,\mu$m feature. Then helium is still a promising candidate to cause strong absorption near $1\,\mu$m for these subluminous He-shell DDet SNe Ia.

In conclusion, every thick He-shell DDet candidate with available NIR spectra displays a strong absorption feature near $1\,\mu$m. This feature is not seen in normal SNe Ia. Interestingly, the available NIR spectra are all obtained at different epochs, suggesting that this feature may be long lived. If the feature is due to He I, then DDet explosions exhibit a wide diversity in the expansion velocity. While it remains to be confirmed in

a larger sample, we speculate that anomalously strong absorption around $1\,\mu$m is a distinctive attribute of He-shell DDet SNe and that this feature can be used to identify and select events relative to normal SNe Ia.

4.3. *The Host Environment of He-Shell DDet SNe*

We model the host galaxy of SN 2020jgb using `prospector` (Johnson et al. 2021), a package for principled inference of stellar population properties using photometric and/or spectroscopic data. `Prospector` applies a nested sampling fitting routine through `dynesty` (Speagle 2020) to the observed data and produces posterior distributions of the stellar population properties and model spectral energy distributions (SEDs) with use of `Python-FSPS` (Conroy et al. 2009; Conroy & Gunn 2010). Our observed data include the Galactic-extinction-corrected DEIMOS spectrum, as well as the archival photometric data from the Panoramic Survey Telescope and Rapid Response System (Pan-STARRS; Chambers et al. 2016, g, r, i, z, y Kron magnitudes) and the VISTA Hemisphere Survey (VHS; McMahon et al. 2013, J and K_s Petrosian magnitudes). We use a parametric delayed-τ star-formation history, given by Equation (1) of Nugent et al. (2020) and defined by the e-folding factor τ, the Galactic dust extinction law (Cardelli et al. 1989), and the Chabrier initial mass func-
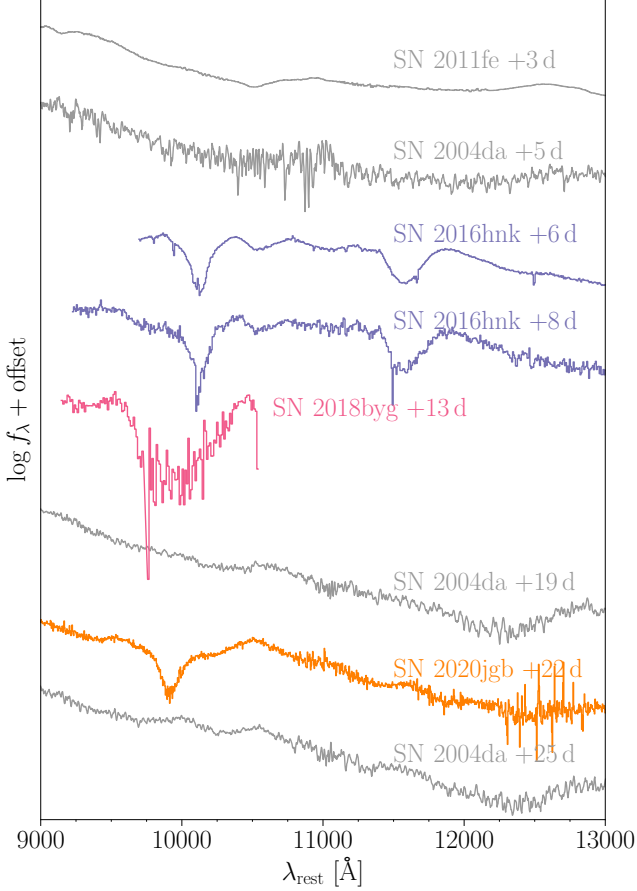
Figure 5. NIR spectra of normal SNe Ia SN 2011fe (Mazzali et al. 2014) and SN 2004da (Marion et al. 2009) and three subluminous SNe Ia as He-shell DDet candidates — SN 2016hnk (Galbany et al. 2019), SN 2018byg (De et al. 2019), and SN 2020jgb (this work). All three He-shell DDet candidates show prominent absorption near $1\,\mu m$. The spectrum of SN 2018byg is originally noisy, so it is binned with a size of $10\,\text{Å}$.

tion (Chabrier 2003) to the model. We further apply a mass-metallicity relation (Gallazzi et al. 2005) to sample realistic stellar masses and metallicities and a dust law that ensures young stellar light attenuates dust twice the amount of old stellar light, as has been observed. We also add a nebular emission model with a gas-phase metallicity and a gas ionization parameter to correctly measure the strength of the emission lines in the DEIMOS spectrum. The model spectral continuum is built from a tenth-order Chebyshev polynomial. We determine the stellar mass and star-formation rate (SFR) from the `prospector` output, as shown by Nugent et al. (2022). The estimated stellar mass is $\log(M_* \, [\mathrm{M_\odot}]) = 7.79^{+0.07}_{-0.06}$, and the specific star-formation rate (sSFR) is $\log(\mathrm{sSFR}\,[\mathrm{yr^{-1}}]) = -10.25^{+0.09}_{-0.08}$, with the uncertainties denoting the 68% highest posterior density regions.

In Figure 8, we show the sSFR and the stellar mass for the host galaxies of six He-shell DDet candidates. Again using `prospector`, we fit the stellar properties for all the other candidates with optical spectra from the Sloan Digital Sky Survey (SDSS; York et al. 2000) and photometry from the DESI Legacy Imaging Surveys (Dey et al. 2019, g, r, z, W_1, W_2, W_3, W_4 magnitudes). With mid-infrared (MIR) photometry available, `prospector` can better estimate the overall dust extinction in the host galaxy and the contribution of an active galactic nucleus (AGN) to the SED. We therefore add two additional parameters to our `prospector` fit to sample the MIR optical depth and fraction of AGN luminosity. Unfortunately, two hosts (those of SN 2016hnk and SN 2019ofm) are nearby ($z \lesssim 0.03$) late-type galaxies with extended, spatially resolved spiral structures. Examination of the photometry model from Legacy Surveys (LS) shows that the galaxy aperture does not include the blue, diffuse star-forming regions of these galaxies. Fitting the SDSS spectra + LS photometry would inevitably underestimate their sSFR. For the host of SN 2016hnk, we instead adopt the results of Dong et al. (2022b), which uses broadband far-ultraviolet (FUV) to far-infrared (FIR) photometry from the $z = 0$ Multiwavelength Galaxy Synthesis I (z0MGS; Leroy et al. 2019) to characterize the stellar population with `prospector`. For the host of SN 2019ofm, there are no archival stellar population data available; so, we still show our best-fit parameters in Figure 8, with the caveat that the sSFR should be regarded as a lower limit. In addition, the host of SN 2018aoz (NGC 3923) is a local ($z = 0.00580$) early-type galaxy and is outside the SDSS footprint, so we adopt its stellar population properties from the Census of the Local Universe (CLU) catalog (Cook et al. 2019; De et al. 2020). PTF 09dav is not displayed in Figure 8 because it appears to be hostless, with the nearest galaxy with a known redshift being a star-forming late-type galaxy $\sim$40 kpc away (Sullivan et al. 2011). Nonetheless, it is close to several extended sources with low surface brightness, which could be faint dwarf galaxies (see Figure 3 in Kasliwal et al. 2012). Its nebular-phase spectrum exhibits Hα emission, which indicates potential star formation, but could also be explained with photoionized gas around the transient (Kasliwal et al. 2012).

Figure 8 reveals that DDet SNe emerge in both star-forming and passive galaxies, which is true for both thin He-shell objects of normal luminosity (SN 2016jhr in a star-forming host; SN 2018aoz in a passive host) and thick He-shell, subluminous objects (SN 2020jgb in a star-forming host; SN 2018byg in a passive host).
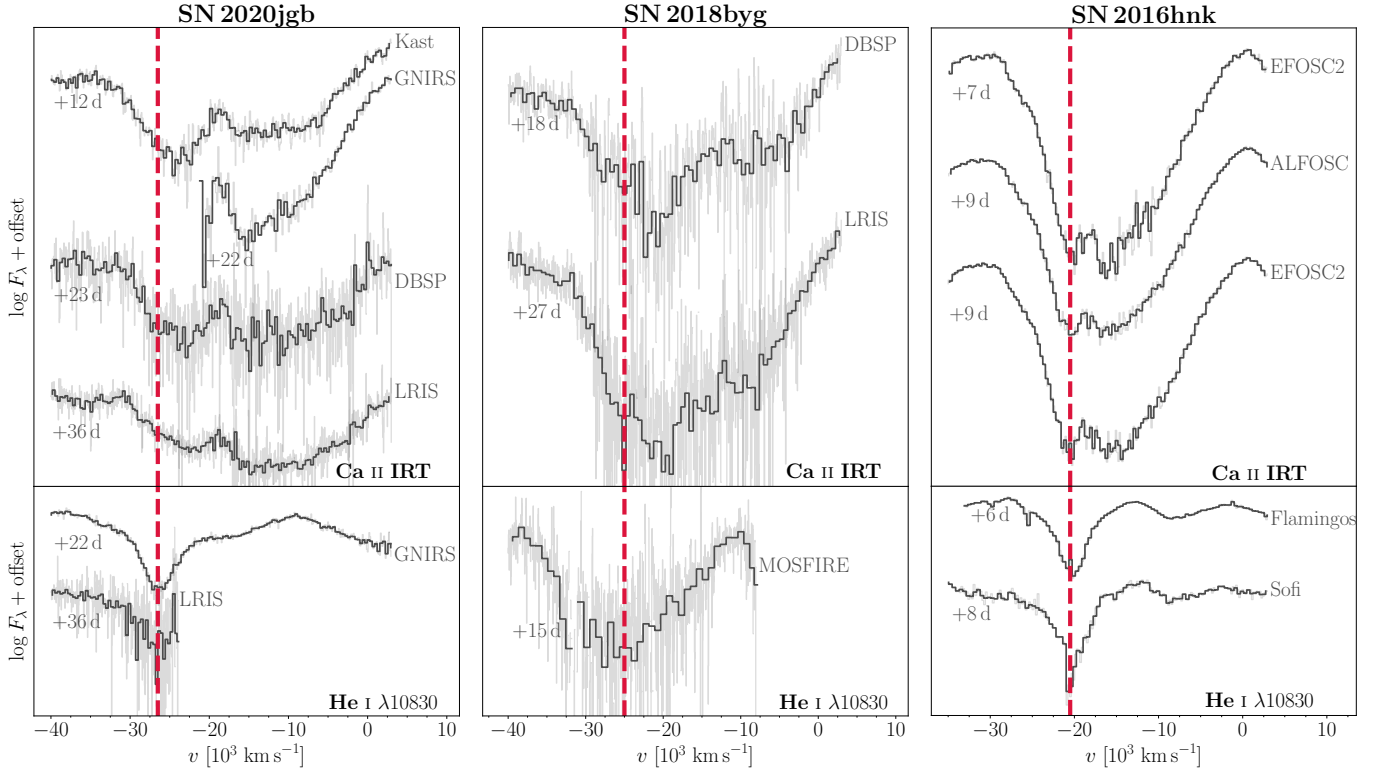
Figure 6. Spectra of SN 2020jgb, SN 2018byg (De et al. 2019), and SN 2016hnk (Galbany et al. 2019) in velocity space, showing the similarity in expansion velocities of the $1\,\mu$m features (lower panels) with the Ca II IRT absorption features (upper panels), assuming the $1\,\mu$m features are associated with He I λ10830. The red dashed lines mark the minimum of each $1\,\mu$m feature, which are displayed to guide the eye.

Their locations in host galaxies also show large variety. SN 2020jgb has a small projected physical offset ($\sim$0.2 kpc) from the center of its host, a star-forming dwarf galaxy, so it is likely to originate from a young, star-forming environment. SN 2016hnk has a moderate projected host offset ($\sim$4 kpc) and a potential origin in an H II region with ongoing star formation (Galbany et al. 2019). SN 2019ofm has a large projected offset ($\sim$11 kpc) but is still on the blue, diffuse spiral arm, as shown in its DECaLS image (Dey et al. 2019). Other objects, including the recently reported SN 2016dsg and OGLE-2013-SN-079 (Dong et al. 2022a), show large projected host offsets ($\gtrsim$10 kpc) and lie in the galaxy outskirts, which usually indicates origin in an old stellar population.

In this sense, the He-shell DDet sample resembles the normal SN Ia population, which can occur in both star-forming and quenched galaxies (e.g., Sullivan et al. 2006; Smith et al. 2012). This is very different from some other types of thermonuclear SNe such as Type-Iax SNe (SNe Iax), which almost only appear in star-forming galaxies, or 91bg-like and 02es-like (Ganeshalingam et al. 2012) objects, which prefer old stellar environments (see the review by Jha et al. 2019). This favors the postulated sequence that He-shell DDet SNe may

make up a substantial fraction of normal SNe Ia, and is supported by stellar-metallicity observations (Sanders et al. 2021; Eitner et al. 2022).

The diversities in host environments indicate multiple formation channels in the He-shell DDet SN population. Those in star-forming environments, SN 2020jgb being the most unambiguous example, could originate from some analogues of the two subdwarf B binaries with WD companions (Geier et al. 2013; Kupfer et al. 2022) discovered in young stellar populations. On the other hand, those with large host offsets could not be easily formed *in situ*. Similarly, many Ca-rich transients are also observed in remote locations (Lunnan et al. 2017), for which some dynamical formation channels have been proposed. To reach the outskirts of galaxies, WD binaries would need to be ejected by globular clusters (Shen et al. 2019) or supermassive black holes (Foley 2015) before explosions. Given that some Ca-rich transients show characteristic DDet properties (De et al. 2020), these channels may also be applicable to some of the He-shell DDet SNe.

The robust detection of SN 2020jgb in a star-forming region also agrees with independent studies of SN Ia progenitors using stellar-metallicity observations. After measuring the manganese abundance in the Sculp-
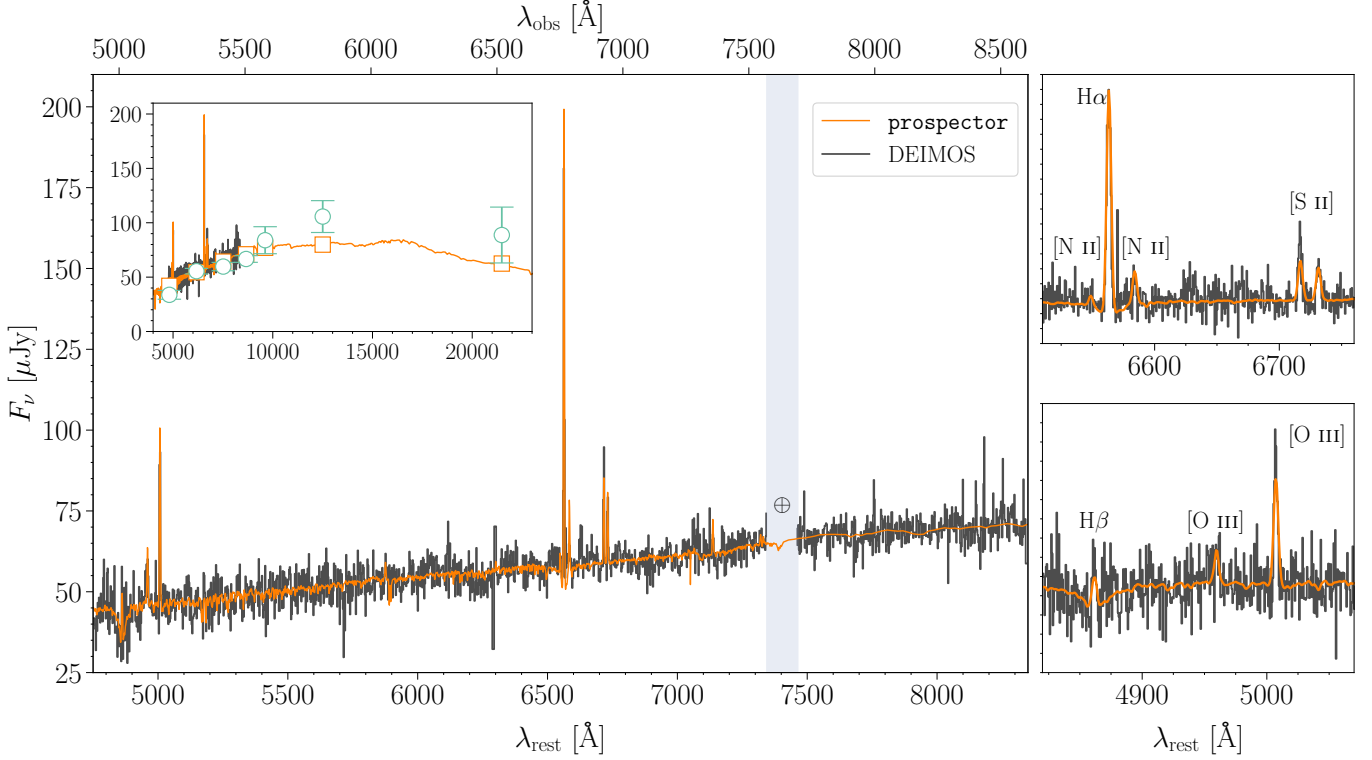
Figure 7. The SED of the star-forming dwarf galaxy PSO J175312.663+005122.078 (the host galaxy of SN 2020jgb) and the model from `prospector`. When fitting the SED with `prospector`, the DEIMOS spectrum is automatically rescaled to fit the archival photometry from Pan-STARRS (Chambers et al. 2016, g, r, i, z, y Kron magnitudes) and VHS (McMahon et al. 2013, J and K_s Petrosian magnitudes). *Left:* the SED in the optical band (4750–8350 Å in the rest frame of the host galaxy). The black line corresponds to the observed spectrum, binned with a size of 2 Å. The orange line is the `prospector` model produced from the median of the stellar population property posterior distributions. The blue shaded region is masked in the fitting owing to the strong telluric lines. *Inner panel:* the same comparison, but covering the g through K_s bands (4000–24,000 Å). Apart from the spectra, we also show the multiband photometry (green circles) and the best-fit magnitudes (orange squares). *Right:* spectra around the most prominent emission lines. *Top right:* Hα, [N II] $\lambda\lambda6548$, 6583, [S II] $\lambda\lambda6716$, 6731. *Bottom right:* Hβ, [O III] $\lambda\lambda4959$, 5007.

tor dwarf spheroidal galaxy, it is argued in de los Reyes et al. (2020) that sub-$M_{\rm Ch}$ SNe Ia dominate the chemical evolution of a galaxy, while near-$M_{\rm Ch}$ SNe tend to take over at later times. This indicates that observationally, sub-$M_{\rm Ch}$ SNe Ia might have a stronger preference toward younger stellar populations than near-$M_{\rm Ch}$ SNe Ia. Since He-shell DDet is one of the most favored channels to ignite a sub-$M_{\rm Ch}$ WD, we would expect that the majority of SNe Ia in star-forming galaxies (at least the dwarfs) would undergo He-shell DDet. We note that while SN 2020jgb is the first confirmed He-shell DDet SN in a star-forming dwarf, which indicates that thick He-shell DDet SNe might be intrinsically rare, the same may not be true for those ignited by a thin He-shell since they would look just as "normal" a few days after explosion (Ni et al. 2022a). Unfortunately, few SNe Ia have been observed at such an early phase to date (SN 2016jhr and SN 2018aoz being two of them); thus, we might have missed a great number of thin He-shell DDet SNe. A sys-

tematic study based on prompt follow-up observations of infant SNe Ia will help verify this implication, with more efficient time-domain surveys in the future.

5. CONCLUSIONS

We have presented observations of SN 2020jgb, a peculiar SN Ia. It has a low luminosity, red $g_{\rm ZTF} - r_{\rm ZTF}$ colors, and strong line-blanketing in the optical spectra near maximum light, all of which are highly similar to SN 2018byg (De et al. 2019), whose observational properties could be explained by the detonation of a shell of helium on a sub-$M_{\rm Ch}$ WD. Fitting the light curves of SN 2020jgb to a grid of models from Polin et al. (2019), we show that a ∼0.87 $M_\odot$ WD beneath a ∼0.08 $M_\odot$ He-shell provides a reasonable match to the observed spectrophotometric evolution of SN 2020jgb.

A high-SNR NIR spectrum obtained three weeks after maximum light exhibits a prominent absorption feature near 1 μm, which could be produced by the unburnt
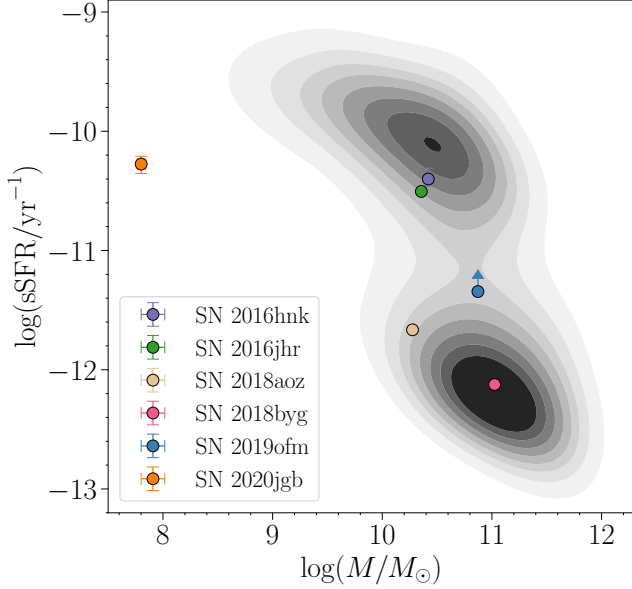
Figure 8. The sSFR and stellar mass for the host galaxies of He-shell DDet candidates, showing that He-shell DDet SNe can emerge in both star-forming and passive galaxies. The properties for the hosts of SN 2016hnk and SN 2018aoz are taken from Dong et al. (2022b) and the CLU catalog (Cook et al. 2019; De et al. 2020), respectively. For the sSFR in the host of SN 2019ofm, only a lower limit is shown (the circle with an arrow). The gray contours correspond to the bivariate distributions of stellar mass and sSFR for galaxies in the SDSS MPA-JHU DR8 catalog (Kauffmann et al. 2003; Brinchmann et al. 2004), visualized using kernel density estimation (KDE) with the data visualization library `seaborn` (Waskom 2021). Galaxies with BPT classification as AGNs or LINERs are excluded, since certain spectral features (e.g., Hα emission) due to nuclear activity might be misinterpreted as being caused by star formation.

helium (He I λ10830) in the outermost ejecta expanding at a high velocity ($\sim$26,000 km s^{-1}). At the same epoch, the Ca II IRT also has similarly high velocities ($\sim$24,000 km s^{-1}). To date, only four candidate He-shell DDet SNe have observed NIR spectra. Interestingly, all of them show deep absorption features near 1 μm, which, if assumed to be He I λ10830, would be expanding at a very similar velocity to the HVFs of Ca II IRT. For these candidates the Ca II HVFs and putative He I velocities show significant diversity ranging from $\sim$15,000 km s^{-1} in SN 2016dsg to $\sim$24,000 km s^{-1} in SN 2020jgb. If it is the unburnt helium and the newly synthesized calcium from the He-shell that produce these line features, such a consistency in the expansion rates of different absorption lines would be naturally explained. However, we could not find unambiguous evidence for other He I absorption lines, such as He I λ20581, so we cannot claim a definitive detection of helium in SN 2020jgb. Nonethe-

less, alternative possibilities (Mg II, C I, Fe II) that may cause the 1 μm feature are deemed even less likely. Helium is thus the most plausible explanation for the apparently ubiquitous 1 μm features.

We propose that He-shell DDet SNe can be robustly identified with NIR spectra. For transients showing a clear 1 μm feature, to test its potential association with He I λ10830 one could follow the checklist below.

- Search for He I λ20581. A caveat is that one should not always expect to see significant He I λ20581 absorption in He-shell DDet SNe, since this line is weaker than He I λ10830 and could be almost invisible when the He-shell is thin (Boyle et al. 2017). The strong telluric lines near 2 μm also add to the difficulty in detecting He I λ20581.

- Calculate the line velocity assuming an origin in He I λ10830 and check if it is comparable with the HVFs velocity in the Ca II IRT absorption at a similar phase. While both the detonation recipe in a He-shell DDet model and the viewing angles would affect the observed He I/Ca II velocity, we still expect the elements along the line of sight to expand at a similar velocity, if they all have a He-shell origin.

- Exclude the possibility of other strong lines. If the NIR spectrum is obtained before the peak brightness of the SN, strong Mg II and C I absorption (Hsiao et al. 2019) would be possible contaminants. Otherwise, if the 1 μm feature is seen in the transitional-phase spectrum when the inner region of the SN becomes visible, we need to carefully rule out the possibility of an Fe II origin (Marion et al. 2009).

The He-shell DDet SNe in the tiny sample show diversities in various observational properties, including the peak luminosity, color evolution, chemical abundances, and line velocities, which could be explained by a large variety of He-shell and WD masses (Polin et al. 2019; Shen et al. 2021), viewing angles (Shen et al. 2021), and the initial chemical compositions in the He-shell (Kromer et al. 2010). In addition, they are discovered in both old and young stellar populations, SN 2020jgb being the first unambiguous thick He-shell DDet candidate in a star-forming galaxy. If, as has been argued (e.g., Sanders et al. 2021; Eitner et al. 2022), a substantial fraction of normal SNe Ia are triggered by He-shell DDet, then we would naturally expect He-shell DDet SNe to emerge in both star-forming and passive galaxies as normal SNe Ia do (e.g., Sullivan et al. 2006; Smith et al. 2012), which is exactly what we observe. This is

unlike some other subtypes of SNe Ia (Jha et al. 2019) which strongly prefer either star-forming galaxies (e.g., SNe Iax) or passive galaxies (e.g., 91bg-like and 02es-like objects). Nonetheless, it remains to be examined whether thick He-shell DDet SNe stem from similar progenitors as the majority of normal SNe Ia, or if their massive He-shells could only be developed in a completely distinctive population of binary systems.

Facility: PO:1.2m (ZTF), PO:1.5m (SEDM), Gemini:Gillett (GNIRS), Hale (DBSP), NOT (ALFOSC), Shane (Kast Double spectrograph), Keck:I (LRIS), Keck:II (DEIMOS).

Software: astropy (Astropy Collaboration et al. 2013, 2018), CASTRO (Almgren et al. 2010), dynesty (Speagle 2020), emcee (Foreman-Mackey et al. 2013), matplotlib (Hunter 2007), prospector (Johnson et al. 2021), PypeIt (Prochaska et al. 2020), pysedm (Rigault et al. 2019), Python-FSPS (Conroy et al. 2009; Conroy & Gunn 2010) scipy (Virtanen et al. 2020), seaborn (Waskom 2021), SEDONA (Kasen et al. 2006).

REFERENCES

Almgren, A. S., Beckner, V. E., Bell, J. B., et al. 2010, ApJ, 715, 1221, doi: 10.1088/0004-637X/715/2/1221

Astropy Collaboration, Robitaille, T. P., Tollerud, E. J., et al. 2013, A&A, 558, A33, doi: 10.1051/0004-6361/201322068

Astropy Collaboration, Price-Whelan, A. M., Sipőcz, B. M., et al. 2018, AJ, 156, 123, doi: 10.3847/1538-3881/aabc4f

Baldwin, J. A., Phillips, M. M., & Terlevich, R. 1981, PASP, 93, 5, doi: 10.1086/130766

Bellm, E. C., Kulkarni, S. R., Graham, M. J., et al. 2019a, PASP, 131, 018002, doi: 10.1088/1538-3873/aaecbe

Bellm, E. C., Kulkarni, S. R., Barlow, T., et al. 2019b, PASP, 131, 068003, doi: 10.1088/1538-3873/ab0c2a

Blagorodnova, N., Neill, J. D., Walters, R., et al. 2018, PASP, 130, 035003, doi: 10.1088/1538-3873/aaa53f

Boyle, A., Sim, S. A., Hachinger, S., & Kerzendorf, W. 2017, A&A, 599, A46, doi: 10.1051/0004-6361/201629712

Brinchmann, J., Charlot, S., White, S. D. M., et al. 2004, MNRAS, 351, 1151, doi: 10.1111/j.1365-2966.2004.07881.x

Bulla, M., Miller, A. A., Yao, Y., et al. 2020, ApJ, 902, 48, doi: 10.3847/1538-4357/abb13c

Cardelli, J. A., Clayton, G. C., & Mathis, J. S. 1989, ApJ, 345, 245, doi: 10.1086/167900

Carrick, J., Turnbull, S. J., Lavaux, G., & Hudson, M. J. 2015, MNRAS, 450, 317, doi: 10.1093/mnras/stv547

Cenko, S. B., Fox, D. B., Moon, D.-S., et al. 2006, PASP, 118, 1396, doi: 10.1086/508366

Chabrier, G. 2003, PASP, 115, 763, doi: 10.1086/376392

Chambers, K. C., Magnier, E. A., Metcalfe, N., et al. 2016, arXiv e-prints, arXiv:1612.05560. https://arxiv.org/abs/1612.05560

Childress, M. J., Filippenko, A. V., Ganeshalingam, M., & Schmidt, B. P. 2014, MNRAS, 437, 338, doi: 10.1093/mnras/stt1892

Childress, M. J., Scalzo, R. A., Sim, S. A., et al. 2013, ApJ, 770, 29, doi: 10.1088/0004-637X/770/1/29

Conroy, C., & Gunn, J. E. 2010, ApJ, 712, 833, doi: 10.1088/0004-637X/712/2/833

Conroy, C., Gunn, J. E., & White, M. 2009, ApJ, 699, 486, doi: 10.1088/0004-637X/699/1/486

Cook, D. O., Kasliwal, M. M., Van Sistine, A., et al. 2019, ApJ, 880, 7, doi: 10.3847/1538-4357/ab2131

Dahiwale, A., & Fremling, C. 2020, Transient Name Server Classification Report, 2020-1624, 1

De, K., Kasliwal, M. M., Polin, A., et al. 2019, The Astrophysical Journal, 873, L18, doi: 10.3847/2041-8213/ab0aec

De, K., Kasliwal, M. M., Tzanidakis, A., et al. 2020, The Astrophysical Journal, 905, 58, doi: 10.3847/1538-4357/abb45c

De, K., Kasliwal, M. M., Tzanidakis, A., et al. 2020, ApJ, 905, 58, doi: 10.3847/1538-4357/abb45c

de los Reyes, M. A. C., Kirby, E. N., Seitenzahl, I. R., & Shen, K. J. 2020, ApJ, 891, 85, doi: 10.3847/1538-4357/ab736f

Deckers, M., Maguire, K., Magee, M. R., et al. 2022, MNRAS, 512, 1317, doi: 10.1093/mnras/stac558

Dessart, L., & Hillier, D. J. 2015, MNRAS, 447, 1370, doi: 10.1093/mnras/stu2520

Dey, A., Schlegel, D. J., Lang, D., et al. 2019, AJ, 157, 168, doi: 10.3847/1538-3881/ab089d

Dong, Y., Valenti, S., Polin, A., et al. 2022a, arXiv e-prints, arXiv:2206.07065. https://arxiv.org/abs/2206.07065

Dong, Y., Milisavljevic, D., Leja, J., et al. 2022b, ApJ, 927, 199, doi: 10.3847/1538-4357/ac5257

Duev, D. A., Mahabal, A., Masci, F. J., et al. 2019, MNRAS, 489, 3582, doi: 10.1093/mnras/stz2357

Eitner, P., Bergemann, M., Ruiter, A. J., et al. 2022, arXiv e-prints, arXiv:2206.10258. https://arxiv.org/abs/2206.10258

Elias, J. H., Vukobratovich, D., Andrew, J. R., et al. 1998, in Society of Photo-Optical Instrumentation Engineers (SPIE) Conference Series, Vol. 3354, Infrared Astronomical Instrumentation, ed. A. M. Fowler, 555–565, doi: 10.1117/12.317281

Faber, S. M., Phillips, A. C., Kibrick, R. I., et al. 2003, in Society of Photo-Optical Instrumentation Engineers (SPIE) Conference Series, Vol. 4841, Instrument Design and Performance for Optical/Infrared Ground-based Telescopes, ed. M. Iye & A. F. M. Moorwood, 1657–1669, doi: 10.1117/12.460346

Filippenko, A. V. 1997, ARA&A, 35, 309,
   doi: 10.1146/annurev.astro.35.1.309

Filippenko, A. V., Chornock, R., Swift, B., et al. 2003,
   IAUC, 8159, 2

Filippenko, A. V., Richmond, M. W., Branch, D., et al.
   1992, AJ, 104, 1543, doi: 10.1086/116339

Fink, M., Röpke, F. K., Hillebrandt, W., et al. 2010, A&A,
   514, A53, doi: 10.1051/0004-6361/200913892

Fitzpatrick, E. L. 1999, PASP, 111, 63, doi: 10.1086/316293

Foley, R. J. 2015, MNRAS, 452, 2463,
   doi: 10.1093/mnras/stv789

Foreman-Mackey, D., Hogg, D. W., Lang, D., & Goodman,
   J. 2013, PASP, 125, 306, doi: 10.1086/670067

Fremling, C. 2020, Transient Name Server Discovery
   Report, 2020-1247, 1

Galbany, L., Ashall, C., Höflich, P., et al. 2019, Astronomy
   & Astrophysics, 630, A76,
   doi: 10.1051/0004-6361/201935537

Gallazzi, A., Charlot, S., Brinchmann, J., White, S. D. M.,
   & Tremonti, C. A. 2005, MNRAS, 362, 41,
   doi: 10.1111/j.1365-2966.2005.09321.x

Ganeshalingam, M., Li, W., Filippenko, A. V., et al. 2012,
   ApJ, 751, 142, doi: 10.1088/0004-637X/751/2/142

Geier, S., Marsh, T. R., Wang, B., et al. 2013, A&A, 554,
   A54, doi: 10.1051/0004-6361/201321395

Graham, M. J., Kulkarni, S. R., Bellm, E. C., et al. 2019,
   PASP, 131, 078001, doi: 10.1088/1538-3873/ab006c

Gronow, S., Collins, C., Ohlmann, S. T., et al. 2020, A&A,
   635, A169, doi: 10.1051/0004-6361/201936494

Hsiao, E. Y., Phillips, M. M., Marion, G. H., et al. 2019,
   PASP, 131, 014002, doi: 10.1088/1538-3873/aae961

Hunter, J. D. 2007, Computing in Science and Engineering,
   9, 90, doi: 10.1109/MCSE.2007.55

Inserra, C., Sim, S. A., Wyrzykowski, L., et al. 2015, ApJL,
   799, L2, doi: 10.1088/2041-8205/799/1/L2

Jacobson-Galán, W. V., Polin, A., Foley, R. J., et al. 2020,
   The Astrophysical Journal, 896, 165,
   doi: 10.3847/1538-4357/ab94b8

Jha, S. W., Maguire, K., & Sullivan, M. 2019, Nature
   Astronomy, 3, 706, doi: 10.1038/s41550-019-0858-0

Jiang, J.-a., Doi, M., Maeda, K., et al. 2017, Nature, 550,
   80, doi: 10.1038/nature23908

Johnson, B. D., Leja, J., Conroy, C., & Speagle, J. S. 2021,
   ApJS, 254, 22, doi: 10.3847/1538-4365/abef67

Kasen, D., Thomas, R. C., & Nugent, P. 2006, ApJ, 651,
   366, doi: 10.1086/506190

Kasliwal, M. M., Kulkarni, S. R., Gal-Yam, A., et al. 2012,
   ApJ, 755, 161, doi: 10.1088/0004-637X/755/2/161

Kauffmann, G., Heckman, T. M., White, S. D. M., et al.
   2003, MNRAS, 341, 33,
   doi: 10.1046/j.1365-8711.2003.06291.x

Kromer, M., Sim, S. A., Fink, M., et al. 2010, ApJ, 719,
   1067, doi: 10.1088/0004-637X/719/2/1067

Kupfer, T., Bauer, E. B., van Roestel, J., et al. 2022, ApJL,
   925, L12, doi: 10.3847/2041-8213/ac48f1

Leroy, A. K., Sandstrom, K. M., Lang, D., et al. 2019,
   ApJS, 244, 24, doi: 10.3847/1538-4365/ab3925

Livne, E. 1990, ApJL, 354, L53, doi: 10.1086/185721

Livne, E., & Arnett, D. 1995, ApJ, 452, 62,
   doi: 10.1086/176279

Lunnan, R., Kasliwal, M. M., Cao, Y., et al. 2017, ApJ,
   836, 60, doi: 10.3847/1538-4357/836/1/60

Maguire, K., Sullivan, M., Pan, Y. C., et al. 2014, MNRAS,
   444, 3258, doi: 10.1093/mnras/stu1607

Mahabal, A., Rebbapragada, U., Walters, R., et al. 2019,
   PASP, 131, 038002, doi: 10.1088/1538-3873/aaf3fa

Maoz, D., Mannucci, F., & Nelemans, G. 2014, ARA&A,
   52, 107, doi: 10.1146/annurev-astro-082812-141031

Marion, G. H., Höflich, P., Gerardy, C. L., et al. 2009, AJ,
   138, 727, doi: 10.1088/0004-6256/138/3/727

Masci, F. J., Laher, R. R., Rusholme, B., et al. 2019, PASP,
   131, 018003, doi: 10.1088/1538-3873/aae8ac

Matheson, T., Filippenko, A. V., Barth, A. J., et al. 2000,
   AJ, 120, 1487, doi: 10.1086/301518

Mazzali, P. A., Benetti, S., Altavilla, G., et al. 2005, ApJL,
   623, L37, doi: 10.1086/429874

Mazzali, P. A., Sullivan, M., Hachinger, S., et al. 2014,
   MNRAS, 439, 1959, doi: 10.1093/mnras/stu077

McMahon, R. G., Banerji, M., Gonzalez, E., et al. 2013,
   The Messenger, 154, 35

Miller, J., & Stone, R. 1994, The Kast Double Spectograph,
   Lick Observatory technical reports (University of
   California Observatories/Lick Observatory).
   https://books.google.com/books?id=QXk2AQAAIAAJ

Ni, Y. Q., Moon, D.-S., Drout, M. R., et al. 2022a, Nature
   Astronomy, doi: 10.1038/s41550-022-01603-4

—. 2022b, arXiv e-prints, arXiv:2206.12437.
   https://arxiv.org/abs/2206.12437

Nomoto, K. 1982a, ApJ, 253, 798, doi: 10.1086/159682

—. 1982b, ApJ, 257, 780, doi: 10.1086/160031

Nugent, A. E., Fong, W., Dong, Y., et al. 2020, ApJ, 904,
   52, doi: 10.3847/1538-4357/abc24a

—. 2022, arXiv e-prints, arXiv:2206.01764.
   https://arxiv.org/abs/2206.01764

Oke, J. B., & Gunn, J. E. 1982, PASP, 94, 586,
   doi: 10.1086/131027

Oke, J. B., Cohen, J. G., Carr, M., et al. 1995, PASP, 107,
   375, doi: 10.1086/133562

Patterson, M. T., Bellm, E. C., Rusholme, B., et al. 2019, PASP, 131, 018001, doi: 10.1088/1538-3873/aae904

Pereira, R., Thomas, R. C., Aldering, G., et al. 2013, A&A, 554, A27, doi: 10.1051/0004-6361/201221008

Polin, A., Nugent, P., & Kasen, D. 2019, ApJ, 873, 84, doi: 10.3847/1538-4357/aafb6a

—. 2021, ApJ, 906, 65, doi: 10.3847/1538-4357/abcccc

Poznanski, D., Ganeshalingam, M., Silverman, J. M., & Filippenko, A. V. 2011, MNRAS, 415, L81, doi: 10.1111/j.1745-3933.2011.01084.x

Prochaska, J. X., Hennawi, J. F., Westfall, K. B., et al. 2020, Journal of Open Source Software, 5, 2308, doi: 10.21105/joss.02308

Prochaska, J. X., Hennawi, J., Cooke, R., et al. 2020, pypeit/PypeIt: Release 1.0.0, v1.0.0, Zenodo, doi: 10.5281/zenodo.3743493

Rigault, M., Neill, J. D., Blagorodnova, N., et al. 2019, A&A, 627, A115, doi: 10.1051/0004-6361/201935344

Sanders, J. L., Belokurov, V., & Man, K. T. F. 2021, MNRAS, 506, 4321, doi: 10.1093/mnras/stab1951

Schlafly, E. F., & Finkbeiner, D. P. 2011, ApJ, 737, 103, doi: 10.1088/0004-637X/737/2/103

Shahbandeh, M., Hsiao, E. Y., Ashall, C., et al. 2022, ApJ, 925, 175, doi: 10.3847/1538-4357/ac4030

Shen, K. J., Boos, S. J., Townsley, D. M., & Kasen, D. 2021, ApJ, 922, 68, doi: 10.3847/1538-4357/ac2304

Shen, K. J., Kasen, D., Miles, B. J., & Townsley, D. M. 2018, ApJ, 854, 52, doi: 10.3847/1538-4357/aaa8de

Shen, K. J., & Moore, K. 2014, ApJ, 797, 46, doi: 10.1088/0004-637X/797/1/46

Shen, K. J., Quataert, E., & Pakmor, R. 2019, ApJ, 887, 180, doi: 10.3847/1538-4357/ab5370

Silverman, J. M., Vinkó, J., Marion, G. H., et al. 2015, MNRAS, 451, 1973, doi: 10.1093/mnras/stv1011

Silverman, J. M., Foley, R. J., Filippenko, A. V., et al. 2012, MNRAS, 425, 1789, doi: 10.1111/j.1365-2966.2012.21270.x

Sim, S. A., Fink, M., Kromer, M., et al. 2012, MNRAS, 420, 3003, doi: 10.1111/j.1365-2966.2011.20162.x

Sim, S. A., Röpke, F. K., Hillebrandt, W., et al. 2010, ApJL, 714, L52, doi: 10.1088/2041-8205/714/1/L52

Smith, M., Nichol, R. C., Dilday, B., et al. 2012, ApJ, 755, 61, doi: 10.1088/0004-637X/755/1/61

Speagle, J. S. 2020, MNRAS, 493, 3132, doi: 10.1093/mnras/staa278

Sullivan, M., Le Borgne, D., Pritchet, C. J., et al. 2006, ApJ, 648, 868, doi: 10.1086/506137

Sullivan, M., Kasliwal, M. M., Nugent, P. E., et al. 2011, ApJ, 732, 118, doi: 10.1088/0004-637X/732/2/118

Veilleux, S., & Osterbrock, D. E. 1987, ApJS, 63, 295, doi: 10.1086/191166

Virtanen, P., Gommers, R., Oliphant, T. E., et al. 2020, Nature Methods, 17, 261, doi: 10.1038/s41592-019-0686-2

Waskom, M. L. 2021, Journal of Open Source Software, 6, 3021, doi: 10.21105/joss.03021

Woosley, S. E., Taam, R. E., & Weaver, T. A. 1986, ApJ, 301, 601, doi: 10.1086/163926

Woosley, S. E., & Weaver, T. A. 1994, ApJ, 423, 371, doi: 10.1086/173813

Yao, Y., Miller, A. A., Kulkarni, S. R., et al. 2019, ApJ, 886, 152, doi: 10.3847/1538-4357/ab4cf5

York, D. G., Adelman, J., Anderson, John E., J., et al. 2000, AJ, 120, 1579, doi: 10.1086/301513

Zackay, B., Ofek, E. O., & Gal-Yam, A. 2016, ApJ, 830, 27, doi: 10.3847/0004-637X/830/1/27